J. Fluid Mech. (2020), *vol.* 890, R4, doi:10.1017/jfm.2020.129



JFM RAPIDS
journals.cambridge.org/rapids

Injection-gas-composition effects on hypersonic boundary-layer transition

Fernando Miró Miró[1,†] **and Fabio Pinna**[1]

[1]Von Kármán Institute for Fluid Dynamics, Rhode-Saint-Genèse 1642, Belgium

(Received 21 November 2019; revised 21 January 2020; accepted 12 February 2020)

The thermal protection system in atmospheric-entry and hypersonic-cruise vehicles are oftentimes designed to ablate during their operation, thus injecting a mixture of various gases with distinct properties into the boundary layer. Such outgassing affects the propagation of instabilities within the boundary layer that ultimately originates the transition to turbulence. This work uses linear stability theory, in combination with the e^N method, to establish the underlying reason for the experimentally observed advancement/delay of transition in sharp slender hypersonic cones, when injecting lighter/heavier gases. Contrary to the current understanding and experimental correlations, this numerical analysis suggests that such a behaviour is not linked to the isolated effect of the injected gas' molar weight, but to its combination with the blowing discontinuity, porosity and the appearance of a shocklet, consequence of the injected gas composition. The shocklet constitutes a density gradient that acts on second-mode instabilities like a thermoacoustic impedance.

Key words: boundary layer stability, compressible boundary layers, transition to turbulence

1. Background

During the decomposition of the thermal protection system (TPS) of space vehicles during atmospheric entry, the gas injected into the boundary layer is a mixture of various species (Bhutta & Lewis 1992) resulting from the decomposition of the resin and the fibres. The properties of these species vary significantly from one to another, ranging from those that are overly lighter than air (such as H) to those that are much heavier (such as CO_2 or C_3). It is therefore important to understand how the transition dynamics vary when injecting gases with different characteristics.

During the 1960s and 1970s, several groups performed experimental campaigns with various gases injected through a porous surface in a slender cone in hypersonic conditions (Schneider 2010). An ablating TPS is typically formed of composite materials, where the resin and fibres decompose at different rates, thus having multiple

† Email address for correspondence: fernando.miro.miro@vki.ac.be

© The Author(s), 2020. Published by Cambridge University Press

https://doi.org/10.1017/jfm.2020.129 Published online by Cambridge University Press

porous-layer characteristics throughout the process – see Milos & Chen (2013). The mentioned experiments, with fixed porous-layer characteristics, therefore resemble a single instance within this process. However, many of them lacked the control of the test conditions that is necessary to come to a conclusion on the implications of such a composition modification. The most rigorous campaigns by Scott (1960), Marvin & Akin (1970) and Stalmach *et al.* (1971), observed that the injection of lighter gases (with a lower molar mass), such as He, moved transition upstream with respect to air injection. Heavier gases, such as CO_2 or $CHClF_2$, had the opposite effect. Marvin & Akin (1970) developed a correlation weighing in also the molar mass of the injected gas, achieving a remarkable scaling of the experimental results. Stalmach *et al.* (1971) then successfully tested this correlation by applying it to other injected gases, different from those employed by Marvin and Akin. These experimental efforts, however, where not followed by a corresponding theoretical analysis providing the causal link observed in the wind-tunnel tests.

More recently a joint experimental–numerical investigation (see Leyva *et al.* (2009) or Jewell *et al.* (2013)) investigated the injection of CO_2 at the high temperatures featured in Caltech's T5 reflected shock tunnel. In such instances, the three excited vibrational modes of the CO_2 molecule were seen to stabilize the flow and lead to a later transition. However, their research interest was focused on the mentioned vibrational-excitation transition delay, rather than on the link between the molar mass of the injected gas and the transition dynamics.

Another recent experimental–numerical study by Miró *et al.* (2019) showed that discontinuous porous layers may advance transition, even when perturbations are locally stabilized above it, due to the excitation of otherwise stable perturbation frequencies. The authors also reported that the porous layer advanced transition differently in the blowing and non-blowing cases, suggesting a non-trivial coupling of the various phenomena. Surface injection was nevertheless seen to be destabilizing in all cases. Qualitatively similar results were obtained by Linn & Kloker (2008) with direct numerical simulations (DNS). However, the mentioned studies were restricted to a homogeneous gas composition, using air both as the injection and the wind-tunnel test gas.

There have also been efforts Lysenko *et al.* (2019) to explore the influence of the injection gas on transition. However, they were restricted to the supersonic regime, with Mach numbers much lower than those explored by Marvin & Akin (1970) or Stalmach *et al.* (1971), and too low to have second-mode instabilities dominate the transition process.

The present work addresses the main mechanisms by revisiting a configuration similar to that of Marvin and Akin, with a study based on linear stability theory. The following sections will separately elaborate on injection composition, surface porosity, transport modelling, and the injection profile and shocklet. The investigation is restricted to two-dimensional, second-mode waves, repeatedly reported to be the dominant instability leading to transition in noisy wind tunnels, such as the NASA Ames 3.5ft wind tunnel used in Marvin and Akin's work – see Miró *et al.* (2019) or Wagner (2015).

2. Test conditions and gas modelling

The test conditions employed for this investigation are summarized in table 1, which, for the sake of completeness, also includes the unit Reynolds number based on the boundary-layer-edge values ($Re_{1e} = \rho_e u_e/\mu_e$) and the ratio between the isothermal

https://doi.org/10.1017/jfm.2020.129 Published online by Cambridge University Press

M_∞ (—)	p_∞ (Pa)	T_∞ (K)	T_w (K)	$Y_{N_2\infty}$ (—)	$Y_{O_2\infty}$ (—)	Re_{1e} (m^{-1})	$T_w/T_{adiab.}$ (—)
7.4	700.85	69.72	293	0.7671	0.2329	11.426×10^6	0.424

TABLE 1. Test conditions.

s	$\mu_{ref\,s}$ (kg m^{-1} s^{-1})	$S_{\mu\,s}$ (K)	$\kappa_{ref\,s}$ (W K^{-1} m^{-1})	$S_{\kappa\,s}$ (K)	$T_{ref\,s}$ (K)	$\mathcal{M}_s$ (kg mol^{-1})	$H_{f\,s}^{298\,K}$ (J mol^{-1})
Ar	2.117×10^{-5}	146.3	0.0164	146.3	273.16	0.03994	0
He	1.865×10^{-5}	72.9	0.1428	187.4	273.16	0.004003	0
Ne	2.975×10^{-5}	64.1	0.0465	88.1	273.16	0.02018	0
N_2	1.656×10^{-5}	104.7	0.02407	178.1	273.16	0.028013	0
O_2	1.919×10^{-5}	125	0.02449	268.8	273.16	0.031999	0
CO_2	1.380×10^{-5}	253	0.0146	939.8	273.16	0.04401	−393472

TABLE 2. Species thermal and transport constants. Sutherland coefficients obtained from the CFD++ database (see Goldberg *et al.* 1997).

wall and the recovery temperatures (T_w/T_{adiab}). The test gas is considered to be a non-reacting mixture of N_2, O_2, and an additional injected gas – He, Ne, Ar or CO_2. Due to the low test enthalpy, one can assume thermal equilibrium, with the thermal properties given by the rigid-rotor and harmonic-oscillator (RRHO) model – see Miró Miró *et al.* (2019) and Miró Miró (2020).

The Sutherland–Wilke (SW) model is employed to retrieve the mixture's transport properties. The coefficients needed for the evaluation of Sutherland's law for each species are obtained from the CFD++ database (see Goldberg *et al.* 1997), and are collected in table 2. The mixture transport properties are computed using the mixture rule proposed by Wilke (1950). The diffusion fluxes are computed by employing the constant-Schmidt model with $Sc = 0.7$.

The laminar base flow (denoted with an overbar: $\bar{q}$) is obtained from either solving the one-temperature multi-species boundary-layer (BL) or Navier–Stokes (NS) equations (see Miró Miró 2020) with frozen species chemical source terms ($\dot{\omega}_s = 0$). The BL solutions are obtained with DEKAF (see Groot *et al.* (2018), Miró Miró *et al.* (2018*a*) or Ch. 7 in Miró Miró (2020)), and the NS solutions with CFD++ (see Goldberg *et al.* 1997).

The subsequent spatial linear stability theory analyses (see Mack 1984) on the perturbation amplitudes (denoted with a tilde: $\tilde{q}$) are performed with the VESTA toolkit (see Pinna 2013), exploiting the extended automatic derivation and implementation capabilities (see Pinna & Groot (2014) and Ch. 8 in Miró Miró (2020)). The base-line set of boundary conditions is the so-called homogeneous stability boundary condition (HSBC). It refers to a standard set of boundary conditions used in multi-species stability analyses (Miró Miró *et al.* 2019), featuring Dirichlet conditions ($\tilde{q} = 0$) for all perturbation amplitudes, both at the free stream and wall boundaries, except for two: the species partial densities at the wall and the wall-normal velocity at the free stream. The former is accounted for by the linearized species wall-normal momentum conservation, and the latter by the linearized mixture continuity equation, evaluated at the corresponding boundary. Alternatively, one may employ the porous stability boundary condition at the wall (PSBC), obtained from generalizing the acoustic admittance treatment proposed by Gaponov (1978)

https://doi.org/10.1017/jfm.2020.129 Published online by Cambridge University Press

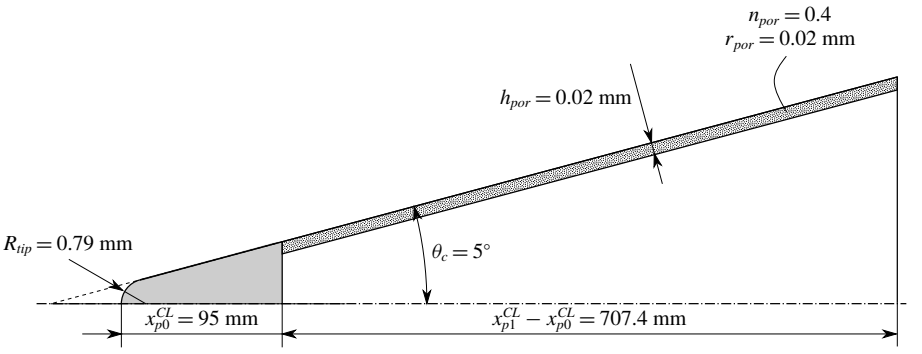


FIGURE 1. Sketch of the cone employed in the investigation, similar to Marvin & Akin (1970).

and Fedorov *et al.* (2001) to multi-species mixtures, as detailed in § 9.2 in Miró Miró (2020). Similarly, one may also impose at the free stream the shock boundary condition, which is the result of linearizing the Rankine–Hugoniot relations across the shock, similarly to Stuckert & Reed (1994) or Pinna & Rambaud (2013) – see Miró Miró (2020). The integration of the N factors for various frequencies of interest, employed in obtaining of the N-factor envelopes, was performed from their neutral point – see Arnal (1993). Verification and validation comparisons for VESTA, DEKAF and CFD++ can be found in the work of Masutti *et al.* (2012), Grossir *et al.* (2014), Martin *et al.* (2019), Miró Miró *et al.* (2018*b*, 2019), Miró *et al.* (2019) or Miró Miró (2020).

Similarly to Marvin & Akin (1970), the selected geometry is a 5-degree half-angle cone, with the physical characteristics summarized in figure 1. Both blunt and infinitely sharp tips are considered, with the former featuring a nose radius of 0.79 mm, equivalent to Marvin and Akin's sharpest tested nose (1/32 in). When employing the PSBC, the porous layer is modelled with the characteristics reported by the authors ($n_{por} = 0.4$ and $h_{por} = 0.02$ mm) and assuming a pore radius of also $r_{por} = 0.02$ mm. The pore radius is not reported, but Dr Marvin suggested, through private communication, that the pore size was sufficiently small, so as to have a uniformly blowing profile. It is therefore taken equal to 20 μm, which, as seen in Miró Miró & Pinna (2018), leads to a minor modification of the stability characteristics when injecting air.

The theoretical characterization of this transpiring cone configuration has multiple aspects that must be considered:

(i) distinct composition of the injected gas;
(ii) transport modelling of a multi-species gas;
(iii) surface's porous characteristics;
(iv) discontinuous blowing;
(v) nose bluntness;
(vi) injection shocklet.

In order to effectively quantify their influence on the development of instabilities, a test matrix considering various geometries, injection profiles and equation systems is presented in table 3. It includes the Heaviside step function $\mathcal{H}(x_0)$, which is 0 for $x < x_0$ and 1 for $x \geqslant x_0$, in order to model a discontinuous mass injection only through the porous section.

https://doi.org/10.1017/jfm.2020.129 Published online by Cambridge University Press

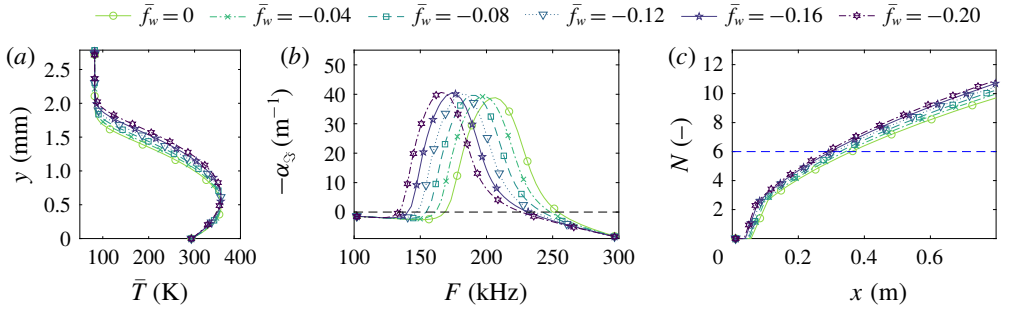


FIGURE 2. Base-flow temperature profiles at $x = 508$ mm (a), second-mode perturbation growth rates at $x = 508$ mm (b), and N-factor envelopes (c) for case 1 (see table 3) with air injection and various values of the self-similar injection parameter.

Case	Tip radius (mm)	$\dot{m}_w(x)$	Eqs.
1	0	cst./$\sqrt{x}$	BL
4	0	cst.$\mathcal{H}(x_{p0})$	NS
5	0.79	cst.$\mathcal{H}(x_{p0})$	NS

TABLE 3. Test matrix. Suffixes 'p' and 's' are added to the case identifier to denote the use of the PSBC and shock boundary condition, rather than the HSBC.

3. Distinct composition of the injected gas

First, the isolated effect of surface injection is explored by comparing the self-similar solution to the boundary-layer equations (case 1 in table 3), varying the blowing parameter $\bar{f}_w$ between 0 (no blowing) and -0.2 (positive blowing). Figure 2 displays the base-flow temperature profiles at $x = 508$ mm (a), together with the perturbation growth rates as a function of the perturbation frequency at that same location (b), and the envelope of the integrated N-factors as a function of the streamwise location (c). One can clearly observe how the larger boundary-layer thickness associated with a stronger blowing (figure 2a) leads to the well-known destabilization of the second mode and the decrease of the unstable frequency range (figure 2b) – see Johnson, Gronvall & Candler (2009), Ghaffari *et al.* (2010) or Miró Miró & Pinna (2018). This ultimately leads to the increase in the N-factor envelopes displayed in figure 2(c). The discontinuous blue line in figure 2(c) and all subsequent N-factor-envelope plots corresponds to an N factor of 6, in the same range as that obtained by Miró *et al.* (2019) in a similar outgassing investigation in the, also noisy, VKI-H3 wind tunnel. It is provided to give an estimation of where one could expect transition to occur under such conditions in an experiment.

The impact of injecting at the wall a gas different than the free stream one, air, (aspect (i) in § 2) is investigated by studying the self-similar solution to the multi-species non-reacting boundary-layer equations (case 1 in table 3). Such a solution is restricted to constant edge quantities (infinitely sharp cone) and blowing parameter $\bar{f}_w$ (implying an injection mass flow that scales like $x^{-1/2}$) (see Miró Miró (2020) or White (1991)).

Figure 3 presents the temperature profile for six different wall concentrations of each of the four injected gases (Y_{sw}), ranging from 0 % to 100 % of the mixture.

https://doi.org/10.1017/jfm.2020.129 Published online by Cambridge University Press

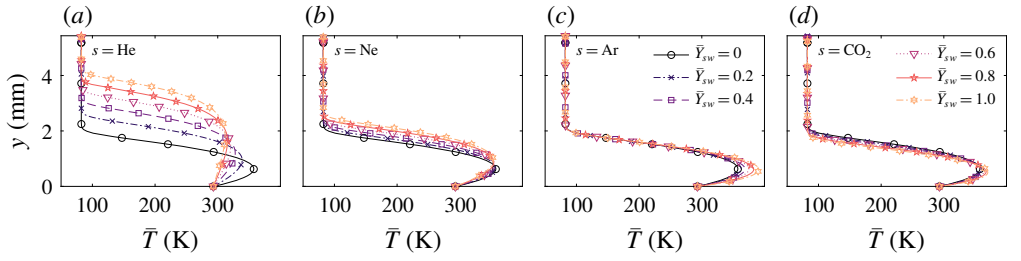


FIGURE 3. Base-flow temperature profiles for case 1 (see table 3) at $x = 508$ mm.

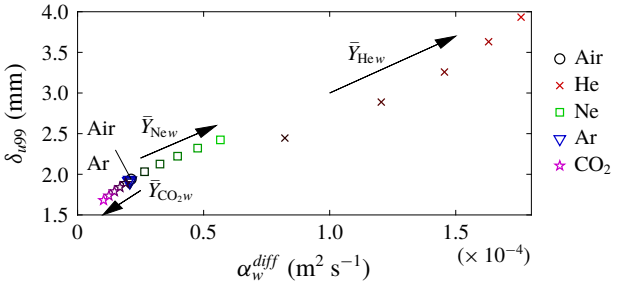


FIGURE 4. Boundary-layer thickness based on 99 % of the edge velocity, for each considered value of the thermal diffusivity at the wall. Different points for the same species correspond to 0 %, 20 %, 40 %, 60 %, 80 % and 100 % of it in the injected gas.

The blowing parameter $\bar{f}_w$ is kept constant for all cases and equal to -0.2, which corresponds to a positive injection velocity v_w. This implies that the injected mass flow remains constant for all the injection-gas compositions, similarly to what was done in the experiments by Marvin & Akin (1970) or Stalmach *et al.* (1971).

The comparison of the boundary-layer profiles in figure 3 suggests that the injection of gases with a higher thermal diffusivity than air (He and Ne) enlarge the boundary-layer thickness, whilst those with a similar one (Ar) do not modify it, and those with a lower one (CO_2) reduce it (see figure 4). The thermal diffusivity is defined as:

$$\alpha^{diff} = \frac{\kappa}{\rho c_p}, \tag{3.1}$$

where κ is the thermal conductivity, ρ is the density and c_p is the heat capacity. It is therefore a measure of how much energy is conducted away, with respect to the energy internally stored by a gas. For the particular problem at hand, a high thermal diffusivity implies that whatever enthalpy difference arises in the flow as a consequence of the injection of an external species, it is mostly conducted away from the wall. This increases accordingly the thermal boundary-layer thickness. Similarly, a low thermal diffusivity implies that such an enthalpy difference remains close to the surface. These traits are clearly distinguishable in the boundary-layer plots of the static-enthalpy difference for the various injection compositions, presented in figure 5. Note that the mentioned enthalpy difference may be due to a variation of the heat capacity (linked to the molar mass) or of the formation enthalpy (see table 2). A more thorough investigation on the influence of various gas properties on film cooling can be found in the work by Keller, Kloker & Olivier (2015).

https://doi.org/10.1017/jfm.2020.129 Published online by Cambridge University Press

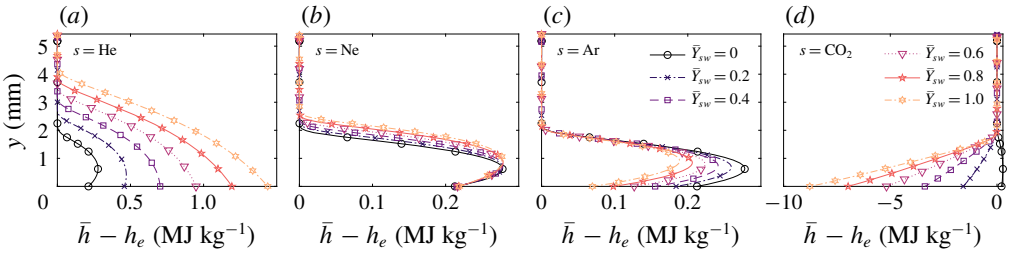


FIGURE 5. Base-flow profiles of the static-enthalpy difference for case 1 (see table 3).

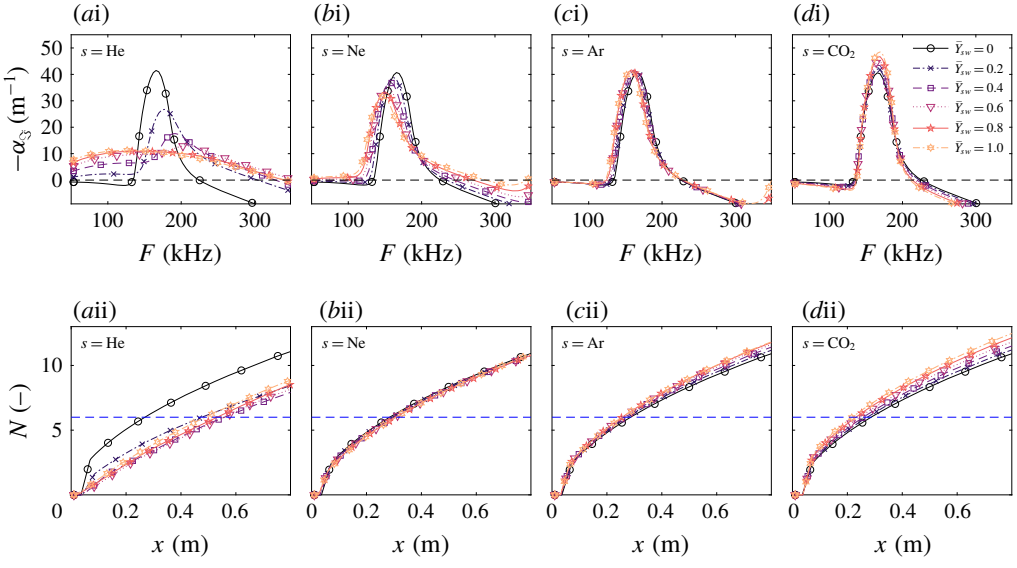


FIGURE 6. Second-mode perturbation growth rates at $x = 508$ mm (i) and N-factor envelopes (ii) for case 1 (see table 3).

Figure 6 displays the corresponding second-mode growth rates at $x = 508$ mm as a function of frequency (i) and the corresponding integrated N-factor envelopes (ii). The growth rates and N-factor envelopes display the opposite trend to what was obtained in the experiments. A higher concentration of lighter gases in the injected mixture leads to less unstable perturbations and lower N factors, whilst a higher concentration of heavier gases has the opposite effect. Observing figure 6(*a*–*b*i), it is clear that, besides lowering the maximum amplification rate, a higher helium or neon concentration at the wall also increases the range of unstable frequencies. One could therefore expect the integration of the N factors to lead to a sooner transition-onset prediction similar to that observed in the experiments. Figure 6(*a*–*d*ii) indeed displays the result of the competing effect of the decrease in the maximum amplification rate (delaying transition) and the widening of the unstable frequency range (advancing transition) for the lighter-gas cases (figure 6*a*–*b*ii). The variation of the wall concentration of neon (figure 6*b*ii) displays a balance of these two effects, which ultimately leads to a negligible change of the predicted transition-onset location. The N-factor envelopes for scenarios injecting heavier gases (figure 6*c*–*d*ii) present

https://doi.org/10.1017/jfm.2020.129 Published online by Cambridge University Press

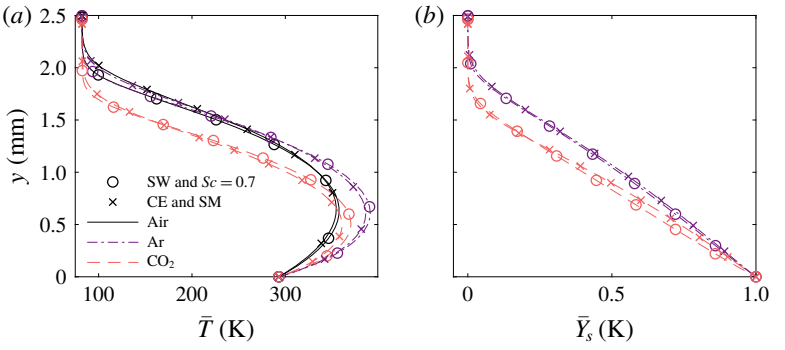


FIGURE 7. Base-flow profiles for case 1 (see table 3) at $x = 508$ mm for two sets of models and various injection gases.

the same trend observed in the growth rates in figure 6(*c–di*): a higher concentration of heavier gases ultimately leads to a sooner predicted transition onset.

One could speculate that the dominant instability, when increasing the concentration of He, is no longer a second mode (see figure 6*ai*). However, varying spanwise-wavenumber analyses discarded this possibility, ensuring that second-mode waves remained dominant.

Overall, the observed trend does not coincide with the experimental findings reported by Marvin & Akin (1970), Scott (1960) and Stalmach *et al.* (1971), being actually opposite to them. This suggests that the advancement/delay of the transition front that they experienced when injecting lighter/heavier gases was not exclusively due to the modification of the injection composition. On the contrary, this effect delays transition for lighter gases and advances it for heavier ones.

4. Transport modelling of a multi-species gas

The dependency of the observed trends on the thermophysical gas modelling (aspect (ii) in § 2) is evaluated by revisiting case 1, yet modifying the transport and the diffusion models for injection mixtures with 100 % of either air, argon or CO_2. Two different sets of models are compared: SW and a constant $Sc = 0.7$ (like in the rest of the article), or Chapman–Enskog (CE) transport and Stefan–Maxwell (SM) diffusion (see Miró Miró *et al.* 2019). For the latter combination, the necessary collisional data are obtained from fitting a polynomial-logarithmic expression to the data in Wright *et al.* (2005), Wright, Hwang & Schwenke (2007). The corresponding curve-fit coefficients are collected in Miró Miró (2020).

One must note that for the considered temperature range (70–400 K), these curve fits are mostly an extrapolation from the original data points. Therefore, the CE and SM models do not offer the higher fidelity, with respect to the SW and the constant $Sc = 0.7$ models, as for high-temperature scenarios – see Miró Miró *et al.* (2019). The comparison displayed in this section thus serves as a metric of the sensitivity of the predictions to modelling variations, and it is not an evaluation of the accuracy achievable with the employed models.

The base-flow profiles obtained with the two sets of models are presented in figure 7. The use of one or another set is seen to have a minor impact on the boundary-layer profiles. It is, however, noteworthy that the CE and SM models predict a stronger cooling and a larger thermal boundary-layer thickness than the

https://doi.org/10.1017/jfm.2020.129 Published online by Cambridge University Press

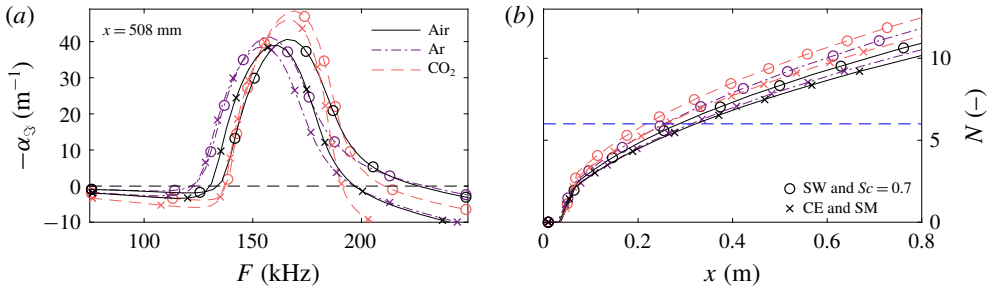


FIGURE 8. Second-mode perturbation growth rates at $x = 508$ mm (a) and N-factor envelopes (b) for case 1 (see table 3) for two sets of models and various injection gases.

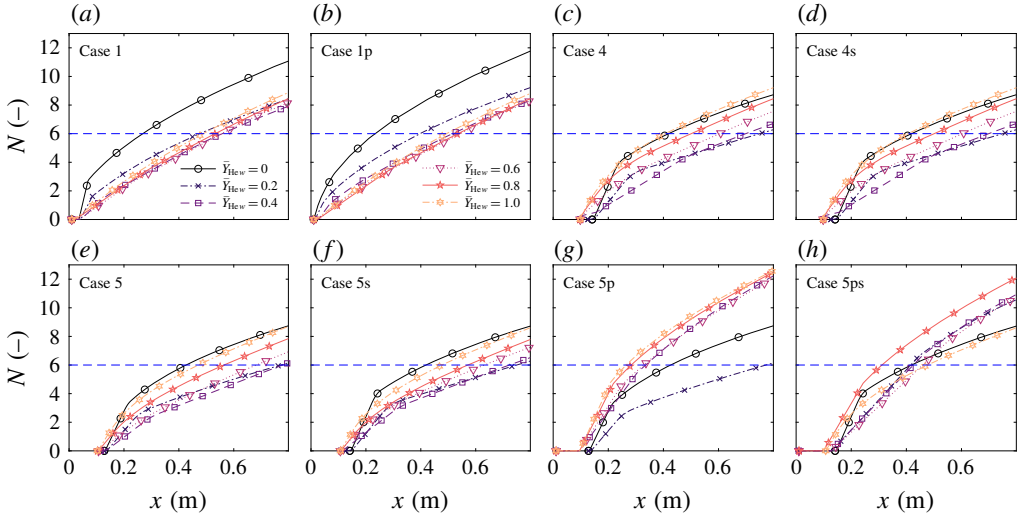


FIGURE 9. Second-mode N-factor envelopes for various cases (see table 3) and He concentrations in the injected mixture.

SW and constant $Sc = 0.7$ models (figure 7*a*). This same trend was reported in Miró Miró *et al.* (2019) when comparing the CE and the Blottner–Eucken–Wilke (BEW) transport models.

Figure 8 displays the second-mode growth rates as a function of frequency at $x = 508$ mm (a) and the integrated N-factor envelopes (b) for the laminar base flow presented in figure 7. The CE and SM models foresee lower growth rates and N factors than the SW and the constant $Sc = 0.7$ models. This shift, however, is consistent across all mixtures. Blowing heavier gases destabilizes the flow, regardless of the transport and diffusion models employed.

It is thus clear that the observed destabilizing effect of injecting heavier gases is independent of the transport and diffusion model.

5. Porosity, discontinuous blowing, nose bluntness, and injection shocklet

Aspects (iii)–(vi) of those listed at the end of § 2 are examined in figure 9. The influence of porosity (iii) on a continuously blowing configuration (case 1) is seen to

https://doi.org/10.1017/jfm.2020.129 Published online by Cambridge University Press

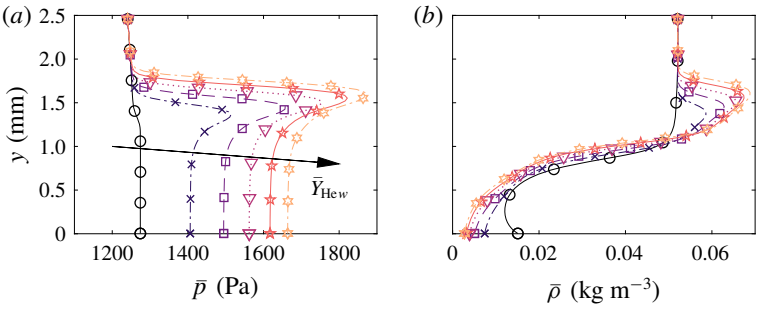


FIGURE 10. Pressure (*a*) and density (*b*) profiles at $x = 0.1$ m showing the injection shocklet for case 5 (see table 3) and for various helium concentrations in the injected mixture.

be negligible, since the *N*-factor envelopes for cases 1 and 1p (the suffix p denotes the PSBC) do not present significant differences (figures 9*a* and 9*b* respectively). However, the combination of the porous boundary condition with a discontinuous blowing can lead to unexpected outcomes because of the competing stabilizing and destabilizing effects – see Miró *et al.* (2019).

The base flows in cases 4 and 5 are obtained from solving the NS rather than the BL equations, and feature a step-wise injection profile. The mass flux is constant ($\dot{\bar{m}}_w = 7.35$ g s^{-1} m^{-2}) in the injection region (see figure 1). The difference between cases 4 and 5 lies in the tip of the cone: infinitely sharp for case 4 and blunt with a nose radius of 0.79 mm for case 5 (the same as in Marvin and Akin's sharpest cone – see figure 1).

A differentiating feature of the cases with a discontinuous mass injection (cases 4 and 5) with respect to case 1 is the appearance of a density gradient at the injection point, translating into a shocklet even if the density gradient is locally negative (see figure 10). The shocklet gradually dissipates as it advances downstream, and is ultimately absorbed by the main shock. The intensity of the shocklet is proportional to the helium concentration in the injected mixture, being almost undetectable when injecting pure air. It is therefore hereinafter referred to as a 'concentration shocklet'.

The existence of this concentration shocklet raises a question regarding its modelling in stability analyses. Since it is a weak shocklet, one could simply keep it within the computational wall-normal domain, and impose a Dirichlet condition at y_{max}, as done in all the other analyses in this article. Another possibility is to restrict the computational domain to the region within the concentration shocklet, and employ the shock perturbation boundary condition on it. The downside to the latter approach is that it neglects the perturbation propagation after the concentration shocklet ($y > y_{shock}$), since the shock boundary condition assumes $\tilde{q} = 0$ in that wall-normal range. However, the advantage is that it does allow for shock oscillation and a coupling with the instabilities. The shock-boundary-condition approach is denoted with the suffix s on the case identifier (for instance case 5 and 5s).

The discontinuous injection of mass through the surface leads to substantially different *N*-factor envelopes. Cases 4 and 5 (figure 9*c* and *e*) present lower *N* factors for the 0 % He-injection case than cases 1 and 1p. However, more significantly, they also present a much larger advancement of the transition front than cases 1 and 1p when increasing $Y_{\mathrm{He}w}$, after the initial delay. This advancement is large enough to have the *N*-factor curve for 100 % He almost coincide with that of 0 % He. This trend

https://doi.org/10.1017/jfm.2020.129 Published online by Cambridge University Press

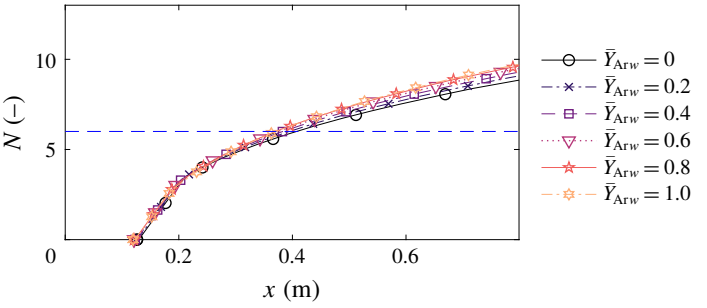


FIGURE 11. Second-mode N-factor envelopes for various case 5p in table 3 with argon injection.

is also almost independent of the strategy employed to deal with the concentration shocklet, since cases 4s and 5s (figure 9*d* and *f*) present almost identical N-factor envelopes to cases 4 and 5 (figure 9*c* and *e*). Moreover, the similarity between the predictions of cases 4 and 5 suggests that the cone's bluntness ($R_{tip} = 0.79$ mm) is not sufficient to modify the dynamics of instability development.

The complete reversal of the trend observed for continuously blowing scenarios with the HSBC, occurs when one considers simultaneously a discontinuous blowing and a PSBC (case 5p in figure 9*g*). This is similar to what was observed in Miró *et al.* (2019), where the porous layer was seen to affect differently the development of instabilities with and without mass injection.

It is interesting, however, to observe that case 5ps in figure 9(*h*) does not predict such a reversal. Case 5ps simultaneously employs the shock boundary condition, truncating the domain at the concentration shocklet, and the porous (PSBC). A possible explanation for this can be given based on the thermoacoustic interpretation of the second mode recently formulated by Kuehl (2018). According to it, the second mode must be interpreted as an acoustic wave confined by the thermoacoustic impedance that is the large density gradient at the top of the boundary layer. The concentration shocklet arising after the injection region (see figure 10) is indeed one of such thermoacoustic impedances.

This impedance is considered by case 5p but not by case 5ps. The use of the shock boundary condition (case 5ps) imposes a different impedance, coming from the linearization of the Rankine–Hugoniot relations. The thermoacoustic coupling of the porous wall and the concentration shocklet appears to increase the growth rates after the injection for lighter gases, and ultimately shifts the corresponding N-factor curves vertically.

Case 5p (discontinuous blowing with a blunt nose and with the PSBC) is also investigated for argon injection, in order to assess whether it is indeed the appropriate modelling strategy or not. The mass flow per unit surface through the porous section is also kept constant and equal to $\dot{\bar{m}}_w = 7.35$ g s^{-1} m^{-2} in the injection streamwise region. The corresponding N-factor envelopes for six different argon concentrations are displayed in figure 11. Similarly to what was observed experimentally by Marvin & Akin (1970), the injection of argon instead of air almost leaves the predicted transition-onset location unchanged. There appears to be a minor advancement associated with higher argon concentrations in the injected mixture. However, this subtle difference could have been inappreciable in the experiments due to the measurement uncertainty.

https://doi.org/10.1017/jfm.2020.129 Published online by Cambridge University Press

6. Conclusions

A thorough investigation was carried out on the sensitivity to the composition of the injected gas of the stability characteristics of wall-bleeding boundary layers, and the ultimately predicted transition-onset location. When injecting mass through the surface in a continuous fashion, lighter gases were seen to increase the boundary-layer thickness, stabilize the second mode, and ultimately lead to a later transition. Heavier gases were seen to have the opposite effect.

Previous wind-tunnel tests, however, do not feature continuously blowing surfaces, but rather a step-wise blowing – zero near the tip and constant after a certain streamwise distance x_{p0}. Experiments in such conditions actually displayed the opposite trend – lighter injection gases led to a sooner transition than heavier gases. The discontinuous blowing is seen to originate a weak shocklet, even if the density gradient is locally negative. The shocklet gets stronger with increasing difference between the mixture molar weights of the incoming and the blown gases. This concentration shocklet acts as a thermoacoustic impedance at a certain height in the domain, and coupled with the admittance of the porous wall, leads to a stronger destabilization when injecting lighter gases. This destabilization ultimately leads to a sooner transition.

The comparison of the predictions made with two distinct sets of transport and diffusion models dismissed the possibility of the heavy-gas destabilization, obtained in the numerical analysis, being an artefact of the thermophysical modelling.

Applying the same hypotheses to a different injection gas (argon) also leads to transition-onset predictions in agreement with the experimental trends, reinforcing the idea that it is indeed the correct way to model the problem at stake. Accounting for the impedance of the porous surface and the discontinuity in the injection profile, and including the thermoacoustic impedance arising from the concentration shocklet within the computational domain, predicts an advancement of the transition-onset location when increasing the concentration of helium in the injection mixture, whilst it remains almost unchanged when increasing the concentration of argon. These predictions qualitatively coincide with the experimental results reported by Marvin & Akin (1970) and Stalmach *et al.* (1971).

Acknowledgement

The authors want to acknowledge the Belgian FNRS for supporting this work through the FRIA fellowship.

Declaration of interests

The authors report no conflict of interest.

References

ARNAL, D. 1993 Boundary layer transition: predictions based on linear theory. In *Special Course on Progress in Transition Modelling AGARD 793*.

BHUTTA, B. A. & LEWIS, C. H. 1992 Low-to-high altitude predictions of three-dimensional ablative reentry flowfields. *AIAA Paper* 92-0366.

FEDOROV, A. V., MALMUTH, N. D., RASHEED, A. & HORNUNG, H. G. 2001 Stabilization of hypersonic boundary layers by porous coatings. *AIAA J.* **39** (4), 605–610.

GAPONOV, S. A. 1978 Effect of the properties of a porous coating on boundary layer stability. *Tech. Rep.* TM 75235, NASA, Santa Barbara, CA.

https://doi.org/10.1017/jfm.2020.129 Published online by Cambridge University Press

GHAFFARI, S., MARXEN, O., IACCARINO, G. & SHAQFEH, E. S. G. 2010 Numerical simulations of hypersonic boundary-layer instability with wall blowing. *AIAA Paper* 2010-706.

GOLDBERG, U., PEROOMIAN, O., CHAKRAVARTHY, S. & SEKAR, B. 1997 Validation of CFD++ code capability for supersonic combustor flowfields. *AIAA Paper* 1997-3271.

GROOT, K. J., MIRÓ MIRÓ, F., BEYAK, E. S., MOYES, A. J., PINNA, F. & REED, H. L. 2018 DEKAF: spectral multi-regime basic-state solver for boundary layer stability. *AIAA Paper* 2018-3380.

GROSSIR, G., PINNA, F., BONUCCI, G., REGERT, T., RAMBAUD, P. & CHAZOT, O. 2014 Hypersonic boundary layer transition on a 7 degree half-angle cone at Mach 10. *AIAA Paper* 2014-2779.

JEWELL, J. S., WAGNILD, R. M., LEYVA, I. A., CANDLER, G. V. & SHEPHERD, J. E. 2013 Transition within a hypervelocity boundary layer on a 5-degree half-angle cone in air/CO_2 mixtures. *AIAA Paper* 2013-0523.

JOHNSON, H. B., GRONVALL, J. E. & CANDLER, G. V. 2009 Reacting hypersonic boundary layer stability with blowing and suction. *AIAA Paper* 2009-938.

KELLER, M. A., KLOKER, M. J. & OLIVIER, H. 2015 Influence of cooling-gas properties on film-cooling effectiveness in supersonic flow. *J. Spacecr. Rockets* **52** (5), 1443–1455.

KUEHL, J. J. 2018 Thermoacoustic interpretation of second-mode instability. *AIAA J.* **56** (9), 3585–3592.

LEYVA, I. A., LAURENCE, S. J., BEIERHOLM, A. W.-K., HORNUNG, H. G., WAGNILD, R. M. & CANDLER, G. V. 2009 Transition delay in hypervelocity boundary layers by means of CO_2/acoustic instability interactions. *AIAA Paper* 2009-1287.

LINN, J. & KLOKER, M. J. 2008 Numerical investigations of film cooling and its influence on the hypersonic boundary-layer flow numerical investigations of film cooling and its influence on the hypersonic boundary-layer flow. In *RESPACE - Key Technologies for Reusable Space Systems* (ed. A. Glhan), pp. 151–169. Springer.

LYSENKO, V. I., GAPONOV, S. A., SMORODSKY, B. V., YERMOLAEV, Y. G. & KOSINOV, A. D. 2019 Influence of distributed heavy-gas injection on stability and transition of supersonic boundary-layer flow. *Phys. Fluids* **31** (10), 104103.

MACK, L. M. 1984 Boundary-layer linear stability theory. In *Special Course on Stability and Transition of Laminar Flow, AGARD 709*.

MARTIN, N., GROSSIR, G., MIRÓ MIRÓ, F., LE QUANG, D. & CHAZOT, O. 2019 Implementation of a laser-based schlieren system for boundary layer instability investigation in the VKI H3 hypersonic wind tunnel. *AIAA Paper* 2019-0624.

MARVIN, J. G. & AKIN, C. M. 1970 Combined effects of mass addition and nose bluntness on boundary-layer transition. *AIAA J.* **8** (5), 857–863.

MASUTTI, D., PINNA, F., GUNAYDINOGLU, E., SOPEK, T. & CHAZOT, O. 2012 Natural and induced transition on a 7deg half-cone at Mach 6. In *RTO-AVT-200*. NATO-RTO.

MILOS, F. S. & CHEN, Y. K. 2013 Ablation, thermal response, and chemistry program for analysis of thermal protection systems. *J. Spacecr. Rockets* **50** (1), 137–149.

MIRÓ, F. M., DEHAIRS, P., PINNA, F., GKOLIA, M., MASUTTI, D., REGERT, T. & CHAZOT, O. 2019 Effect of wall blowing on hypersonic boundary-layer transition. *AIAA J.* **57** (4), 1567–1578.

MIRÓ MIRÓ, F. 2020 Numerical investigation of hypersonic boundary-layer stability and transition in the presence of ablation phenomena. PhD thesis, Université Libre de Bruxelles and von Kármán Insitute for Fluid Dynamics.

MIRÓ MIRÓ, F., BEYAK, E. S., MULLEN, D., PINNA, F. & REED, H. L. 2018*a* Ionization and dissociation effects on hypersonic boundary-layer stability. In *31st ICAS Congress*. International Council of the Aeronautical Sciences.

MIRÓ MIRÓ, F., BEYAK, E. S., PINNA, F. & REED, H. L. 2019 High-enthalpy models for boundary-layer stability and transition. *Phys. Fluids* **31**, 044101.

MIRÓ MIRÓ, F. & PINNA, F. 2018 Effect of uneven wall blowing on hypersonic boundary-layer stability and transition. *Phys. Fluids* **30**, 084106.

MIRÓ MIRÓ, F., PINNA, F., BEYAK, E. S., BARBANTE, P. & REED, H. L. 2018*b* Diffusion and chemical non-equilibrium effects on hypersonic boundary-layer stability. *AIAA Paper* 2018-1824.

https://doi.org/10.1017/jfm.2020.129 Published online by Cambridge University Press

PINNA, F. 2013 VESTA toolkit: a software to compute transition and stability of boundary layers. *AIAA Paper* 2013-2616.

PINNA, F. & GROOT, K. J. 2014 Automatic derivation of stability equations in arbitrary coordinates and different flow regimes. *AIAA Paper* 2014-2634.

PINNA, F. & RAMBAUD, P. 2013 Effects of shock on hypersonic boundary layer stability. *Progr. Flight Phys.* **5**, 93–106.

SCHNEIDER, S. P. 2010 Hypersonic boundary-layer transition with ablation and blowing. *J. Spacecr. Rockets* **47** (2), 225–237.

SCOTT, C. J. 1960 Experimental investigations of laminar heat transfer and transition with foreign gas injection of a 16-deg porous cone at $M = 5$. *Tech. Rep.* UMRAL RR 174, University of Minnesota, Institute of Technology, Rosemony Aeronautical Laboratories, Minneapolis, MN.

STALMACH, C. J. JR., BERTIN, J. J., POPE, T. C. & MCCLOSKEY, M. H. 1971 A study of boundary layer transition on outgassing cones in hypersonic flow. *Tech. Rep.* CR-1908, NASA.

STUCKERT, G. & REED, H. L. 1994 Linear disturbances in hypersonic, chemically reacting shock layers. *AIAA J.* **32** (7), 1384–1393.

WAGNER, A. 2015 The role of carbon/carbon composites in the delay of hypersonic laminar to turbulent boundary layer transition. In *NATO-STO-AVT-261*. NATO-STO.

WHITE, F. 1991 *Viscous Fluid Flow*. McGraw-Hill.

WILKE, C. R. 1950 A viscosity equation for gas mixtures. *J. Chem. Phys.* **18** (4), 517–519.

WRIGHT, M. J., BOSE, D., PALMER, G. E. & LEVIN, E. 2005 Recommended collision integrals for transport property computations. Part I. Air species. *AIAA J.* **43** (12), 2558–2564.

WRIGHT, M. J., HWANG, H. H. & SCHWENKE, D. W. 2007 Recommended collision integrals for transport property computations. Part II. Mars and Venus entries. *AIAA J.* **45** (1), 281–288.

https://doi.org/10.1017/jfm.2020.129 Published online by Cambridge University Press